Cu-loaded polyurethane to reduce ureteral stent microbes adherence and regulation of the inflammation response to RAW264.7

Hongwei Li[1,2], Jing Zhao[3]*, Zhenyu Wang[2], Jiyuan Hu[3],
Jinlong Zhao[3], Bukola O. Awonusi[3], Jianzhong Li[2]* and
Lianhui Fan[1,2]*

[1]Department of Urology, Jinzhou Medical University Graduate Training Base, General Hospital of Northern
Theater Command, Shenyang, China, [2]Department of Urology, General Hospital of Northern Theater
Command, Shenyang, China, [3]Institute of Metal Research, Chinese Academy of Sciences, Shenyang, China

Introduction: Ureteral stents blocked with encrustation are a common clinical complication and affect bacteria colonization and inflammatory response. In this study, different concentrations of copper (0.25, 0.5, 1, 1.5, and 2 g/L) were immobilized on polyurethane (PU) that showed functionalization of microbe resistance and regulation of the inflammation response to RAW264.7.

Methods: X-ray photoelectron spectroscopy (XPS), atomic force microscope (AFM) and static water contact angles were used to analyze the surface characterization. *Proteus mirabilis* resistance test and adhesion of cells by SEM were carried out to evaluate the antibacterial property of Cu-bearing samples. Cell cytotoxicity assay and apoptosis were used to obtain acceptable concentrations of PU-Cu. The morphology of cells was used to observe the occurrence of pseudopodia after contact with PU-Cu. Would healing assay and Transwell invasion assay were carried out to observe the migration and recovery of macrophages. IL-6 and IL-10 were used to evaluate the secretion of pro-/anti-inflammatory cytokines.

Results: X-ray photoelectron spectroscopy (XPS), atomic force microscope (AFM), and static water contact angle measurement were used to confirm successful immobilization of Cu on PU. Plate counting assay and observation of adhered cells by SEM demonstrated that the antibacterial performance of PU-Cu against Proteus mirabilis increased with the amount of Cu loading in a dependent manner. Furthermore, the CCK-8 assay and apoptosis test suggested an acceptable cytotoxicity of PU-Cu at concentrations of 0.25, 0.5, and 1 g/L. The morphology of cells observed by SEM showed reduced occurrence of pseudopodia after contact with PU-Cu. Wound healing and transwell invasion assays manifested that migration and recovery of macrophages were improved by PU-Cu. ELISA of IL-6 and IL-10 demonstrated that PU-Cu could regulate inflammatory cytokines toward anti-inflammatory functionalization.

KEYWORDS

ureteral stent, copper, microbe resistance, inflammatory response, RAW264.7

1 Introduction

Ureteral stents are considered ideal devices for urolithiasis that have been widely used to maintain the patency of urine from renal to bladder and to relieve obstruction of the urinary tract (Li et al., 2021). However, implantation of a foreign object would cause many complications, such as inflammation, encrustation, and urinary symptoms (Sali and Joshi, 2020). More than 80% of the patients suffer from varying degrees of pains in daily life, attributing to the retention of ureteral stents (Soria et al., 2021). Therefore, it is necessary to solve these side effects by inspecting new comfortable materials.

Encrustation generally occurs on both lumen and outer surfaces of the ureteral stent, aggravated by the accumulation of biofilm formation and indwelling time duration (Barghouthy et al., 2021). It has been shown that organic molecules, glycoproteins, and microbes could adhere to the stent in a short-term period to facilitate crystal deposition (Torrecilla et al., 2020). Ureteral stents tender the surface of substrates and are conducive to formatting microbial immobilization and biofilm formation (Bhardwaj and Ingole, 2022). Urease-positive microbiome (*Proteus*, *Klebsiella*, etc.) predisposes urea to ammonia and contributes to the elevation of urine pH that can accelerate precipitation of minerals from urine and gather on the stent. These complicated conditional films and micro-environment around stents construct a mutual promotion to generate new stones (Wasfi et al., 2020; Tomer et al., 2021). The main components of encrustation are calcium phosphate (CaP) and calcium oxalate monohydrate (COM), a potent type of calcium oxalate (CaOx) (Kram et al., 2022). These nuclei gradually induce the formation of stones that result in several kidney stone diseases and deposition of CaOx crystals in infiltrating macrophages (Singhto and Thongboonkerd, 2018; Zhu et al., 2019).

In addition to lumen blocking, stones can also activate the inflammatory response of the human body and ultimately lead to tissue injury under the control of related inflammatory meditators (Li et al., 2020; Liu et al., 2022a). Macrophages play an important role in the early inflammatory response, and diverse cytokines such as interleukin-6 (IL-6), interleukin-1β (IL-1β), and tumor necrosis factor-α (TNF-α) are secreted (Liu et al., 2022b). Once bacterial colonization and crystal deposition occur on the catheter, chronic infection is caused by macrophages and induces overproduction of reactive oxygen species (ROS), chemokines, and pro-inflammatory cytokines (Xue et al., 2020). Consequently, more immune cells including monocytes, macrophages, and neutrophils can be recruited toward the inflammatory sites. In addition, macrophage-engulfed COM contributes to the activation of pyrin domain-containing protein (NLRP3) that influences the recruitment of leukocytes and regulates the corresponding pro-inflammatory cytokines (Anders et al., 2018; Singhto et al., 2018; Lin et al., 2019). Furthermore, during monocytes phagocytosing crystals, macrophages would be polarized into M_1 and M_2 and affect the inflammatory response (Liang et al., 2021). M_1 macrophages modulate promotion of the deposited crystals *via* regulating inflammation response and ROS by releasing pro-inflammatory cytokines like IL-6, leading to the deposition of crystals. Conversely, M_2 polarization positively alleviates inflammatory response with secretion of anti-inflammatory cytokines like IL-10 that are conducive to tissue-healing and phagocytizing crystals (Liu et al., 2020; Jiang et al., 2021).

In this study, copper immobilized on PU was prepared based on the previous successful performance of Cu-bearing stainless steel that reduces biofilm formation, and it was fabricated by using the

TABLE 1 Chemical components of the artificial urine.

Component	Quantity (g)
NaCl	6.17
NaH$_2$PO$_4$	4.59
Na$_3$C$_6$H$_5$O$_7$	0.944
MgSO$_4$	0.463
Na$_2$SO$_4$	2.408
KCl	4.75
Na$_2$C$_2$O$_4$	0.043
CaCl$_2$	0.638

encrustation deposition method (Zhao et al., 2019). X-ray photoelectron spectroscopy (XPS), atomic force microscope (AFM), and contact angle measurement were used to characterize the surface properties. In order to investigate the inflammation response induced by copper after incubation with RAW264.7, cell proliferation, morphology, invasion, and secretion of pro-/anti-inflammatory cytokines were tested by cell counting kit-8 (CCK-8) assay, flow cytometry, scanning electron microscopy (SEM), transwell invasion assay, and enzyme-linked immunosorbent assay (ELISA).
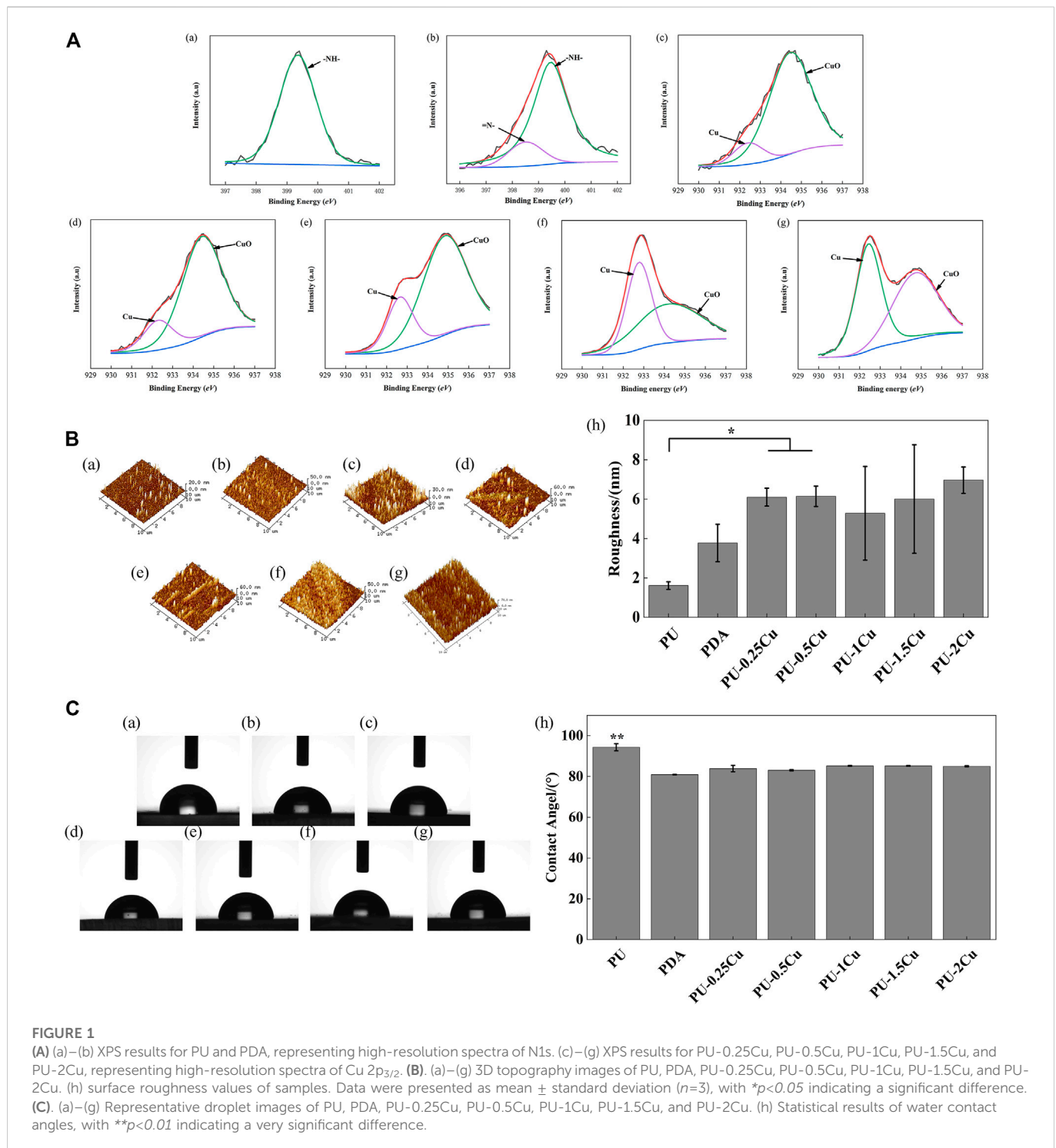
2 Materials and methods

2.1 Preparation of copper-loaded samples

Polyurethanes (PUs) purchased from Lubrizol Corporation (United States) were divided into 10 × 10 mm segments for the experiments. Samples were treated with 2 g/L dopamine hydrochloride (PDA) (Biotopped, China) solution in Tris-HCL buffer at 37 C for 24 h. Then, dopamine-immobilized PU (PU-PDA) was washed ultrasonically with deionized water and absolute ethanol. After drying, the substrates were immersed in different concentrations of CuCl$_2$ (0.25, 0.5, 1, 1.5, and 2 g) solution supplemented with 0.01 mol/L Tris-HCL and 0.1 mol/L dimethylaminoborane (DMAB) (Maya Reagent, China). The copper-bearing specimens were named PU-0.25Cu, PU-0.5Cu, PU-1Cu, PU-1.5Cu, and PU-2Cu according to the concentration of CuCl$_2$.

2.2 Surface characterization

X-ray photoelectron spectroscopy (XPS, Thermo VG, United States) was used to measure the surface chemical compositions of diverse groups of samples with an Al Kα X-ray source. The peaks of copper and N element were analyzed using XPSPEAK41 software. An atomic force microscope (AFM, Agilent 5500) was utilized to detect roughness and surface morphology of coatings. Static water contact angles were measured using a contact angle goniometer (DSA-100, Kruss, Germany) with 5 μL water droplet placed on three random areas of each sample.

FIGURE 1
(A) (a)−(b) XPS results for PU and PDA, representing high-resolution spectra of N1s. (c)−(g) XPS results for PU-0.25Cu, PU-0.5Cu, PU-1Cu, PU-1.5Cu, and PU-2Cu, representing high-resolution spectra of Cu 2p$_{3/2}$. **(B)**. (a)−(g) 3D topography images of PU, PDA, PU-0.25Cu, PU-0.5Cu, PU-1Cu, PU-1.5Cu, and PU-2Cu. (h) surface roughness values of samples. Data were presented as mean $\pm$ standard deviation (n=3), with *$p<0.05$ indicating a significant difference. **(C)**. (a)−(g) Representative droplet images of PU, PDA, PU-0.25Cu, PU-0.5Cu, PU-1Cu, PU-1.5Cu, and PU-2Cu. (h) Statistical results of water contact angles, with **$p<0.01$ indicating a very significant difference.

2.3 *Proteus mirabilis* cultivation and *in vitro* bacteria resistance test

The *Proteus mirabilis* lyophilized powder (BeNa Culture Collection, China) was dissolved in a liquid medium and incubated overnight in a shaker at 150 rpm. Afterward, 100 μL bacterial droplets were cultured on a solid medium for 24 h and prepared for the subsequent test. The plate counting method was used to evaluate the antibacterial property of Cu-bearing samples. A measure of 100 μL

bacterial suspension at a concentration of 5.0×10^5 CFU/mL was dropped on the surface of sterilized samples. After incubating at 37°C for 24 h, samples were transferred into PBS solution and eluted by vortex-mixing for 1 min. The serially diluted suspensions were pipetted out for counting by coating on a solid agar. The antibacterial rate was calculated as follows:

$$\text{Antibacterial rate}\% = \frac{A - B}{A} \times 100\%, \tag{1}$$

TABLE 2 Proportion of Cu element determined by XPS.

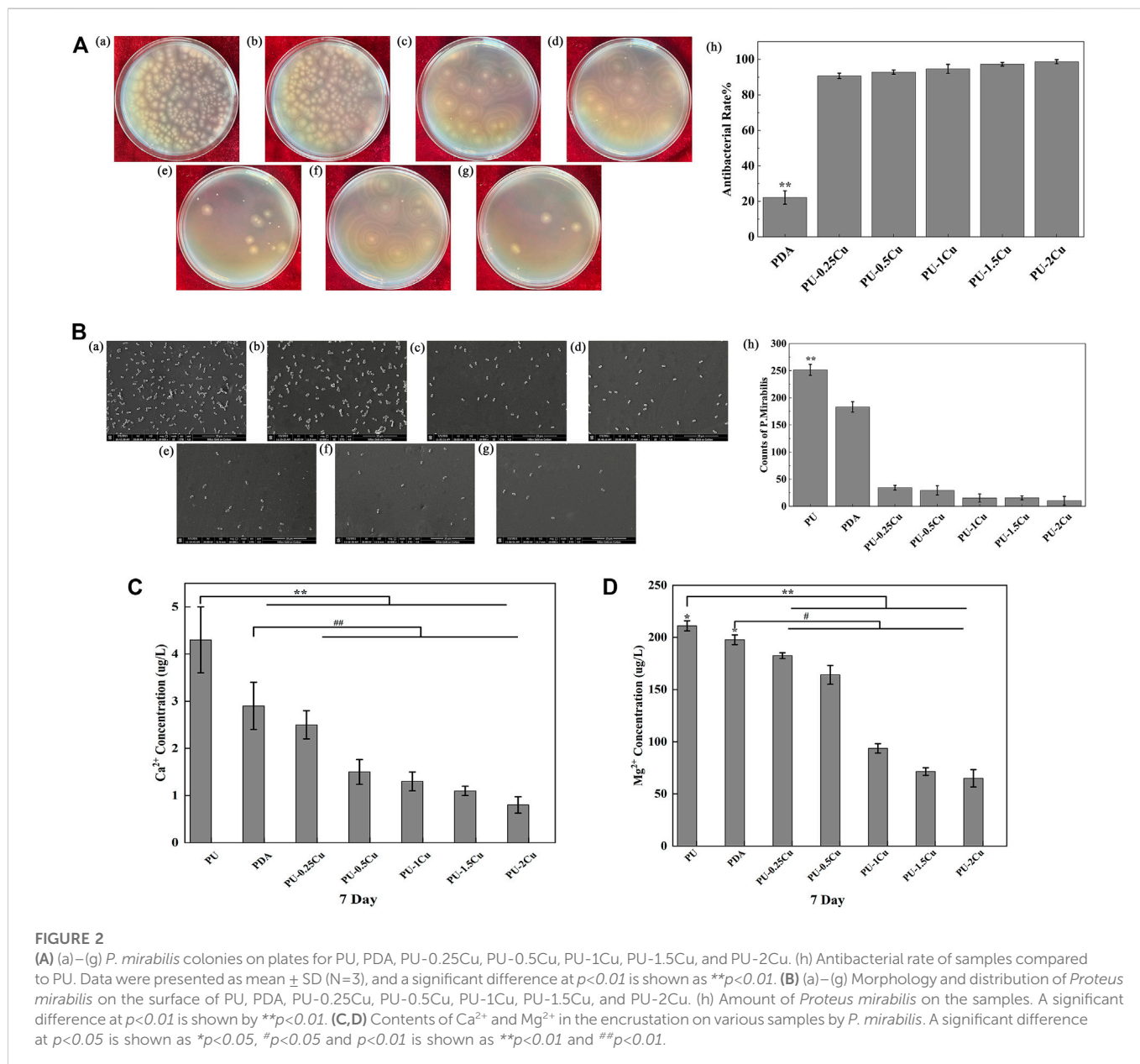| Sample	Cu%
PU-0.25Cu	11.98
PU-0.5Cu	19.09
PU-1Cu	24.61
PU-1.5Cu	46.43
PU-2Cu	51.36

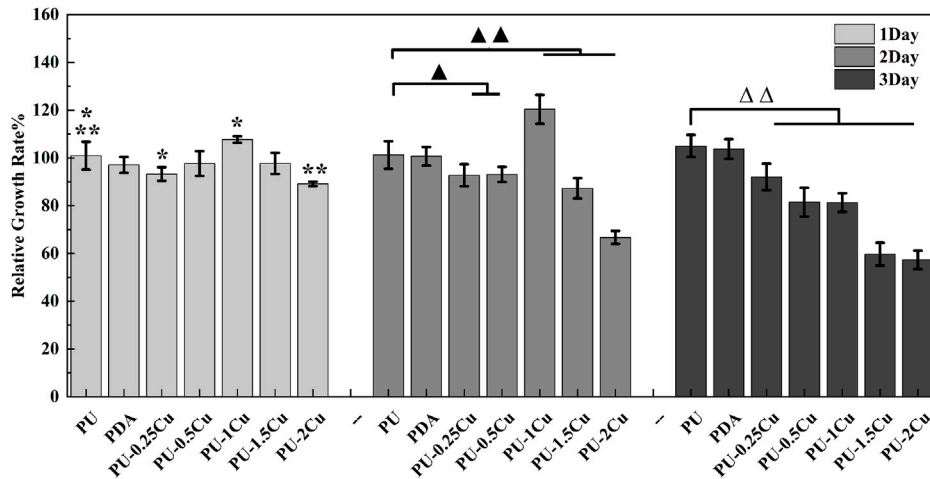where A and B are the colonies of PU and PU-PDA or copper-loaded samples, respectively.

In addition, scanning electron microscopy (TESCAN MIRA, Czech Republic) was used to observe the distribution and morphology of *P. mirabilis* adhered on the substrates incubated with 5.0×10^7 CFU/mL suspensions. After co-culturing for 24 h, samples were washed with PBS three times and then fixed with 2.5% glutaraldehyde (Macklin, China) at 4 C for 2 h. Then, serial dehydration was performed, and samples were dried.

2.4 Deposited encrustation assay

Each sample was immersed in 1 mL artificial urine containing 5.0×10^8 CFU of *P. mirabilis* and then incubated at 37°C for 7 days. The proportion of artificial urine is shown in Table 1. At the indicated time, samples were taken out and washed with deionized water. After immersing in 5% HCl solution and ultrasonically cleaning for 5 min, the contents of Ca^{2+} and Mg^{2+} ions were measured by ICP-MS7900 (Agilent, United States).

FIGURE 2
(A) (a)−(g) *P. mirabilis* colonies on plates for PU, PDA, PU-0.25Cu, PU-0.5Cu, PU-1Cu, PU-1.5Cu, and PU-2Cu. (h) Antibacterial rate of samples compared to PU. Data were presented as mean ± SD (N=3), and a significant difference at $p<0.01$ is shown as **$p<0.01$. **(B)** (a)−(g) Morphology and distribution of *Proteus mirabilis* on the surface of PU, PDA, PU-0.25Cu, PU-0.5Cu, PU-1Cu, PU-1.5Cu, and PU-2Cu. (h) Amount of *Proteus mirabilis* on the samples. A significant difference at $p<0.01$ is shown by **$p<0.01$. **(C,D)** Contents of Ca^{2+} and Mg^{2+} in the encrustation on various samples by *P. mirabilis*. A significant difference at $p<0.05$ is shown as *$p<0.05$, #$p<0.05$ and $p<0.01$ is shown as **$p<0.01$ and ##$p<0.01$.

FIGURE 3
RGR of RAW264.7 cultured with the extracts for 24, 48, and 72 h. Significant differences are marked as *p<0.05*, ▲p<0.05, **p<0.01*, ▲▲p<0.01, and ΔΔp<0.01, respectively.
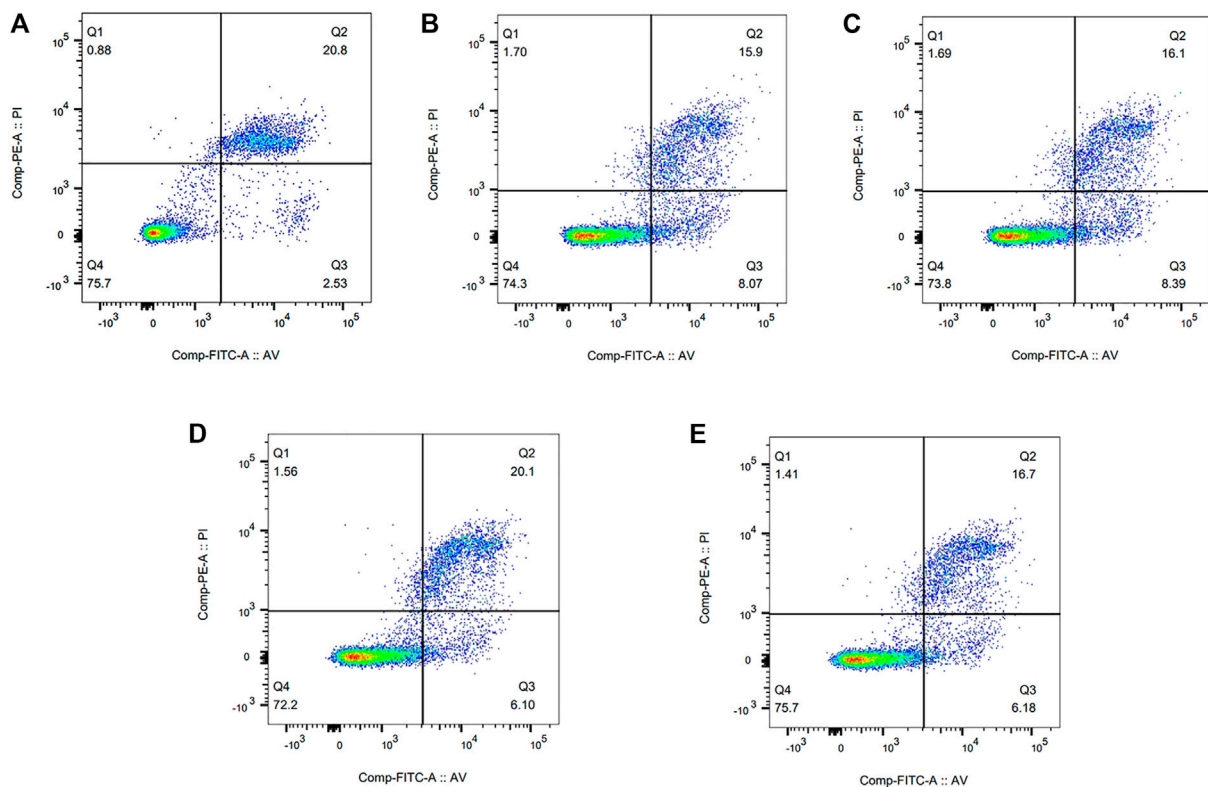
FIGURE 4
Flow cytometry results of RAW264.7 cultured with the extracts for 24 h. **(A)** PU, **(B)** PDA, **(C)** PU-0.25Cu, **(D)** PU-0.5Cu, and **(E)** PU-1Cu.

2.5 RAW264.7 cell line culture

Mouse leukemia cells of monocyte macrophage cell lines (RAW264.7), obtained from the National Collection of Authenticated Cell Cultures, were cultured in Dulbecco's modified Eagle medium (DMEM, HyClone, United States) supplemented with 10% fetal bovine serum (Gibco), 100 U/mL penicillin, and 100 μg/mL streptomycin (Genview, China) in a 5% CO_2 incubator (Shel Lab, United States) at 37 C. Cells were treated with 0.25% trypsin-EDTA (Gibco, Canada) and re-suspended in fresh DMEM, while 80% confluence was reached.
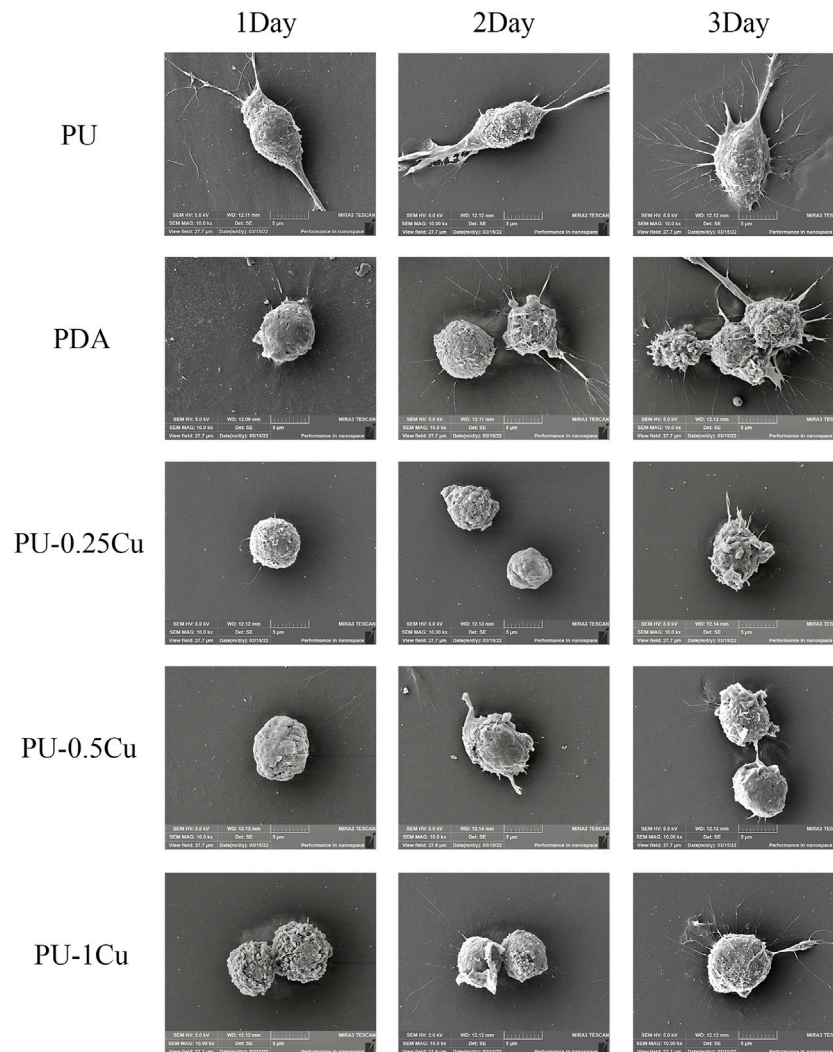
FIGURE 5
SEM images of RAW264.7 on the surface of samples.

2.6 Cytotoxicity assay

Cytotoxicity was used to evaluate the cell viability after treating with 24-h extracts of samples using CCK-8 (Biosharp, China). The ratio of samples' surface-area to culture medium volume (3 cm²/mL) was used to prepare the extracts according to ISO 10993-5. A measure of 100 µL of cell suspensions at a concentration of 3×10^4/mL was seeded in a 96-well plate and incubated overnight. Afterward, the medium was replaced with 100 µL extracts or DMEM (negative control). After 24, 48, and 72 h of incubation, cell counting kit-8 was added and co-cultured for 2 h to measure the optical density (*O.D.*) at 450 nm (Bio-Rad, United States). The relative growth rate (RGR) was calculated by the following equation:

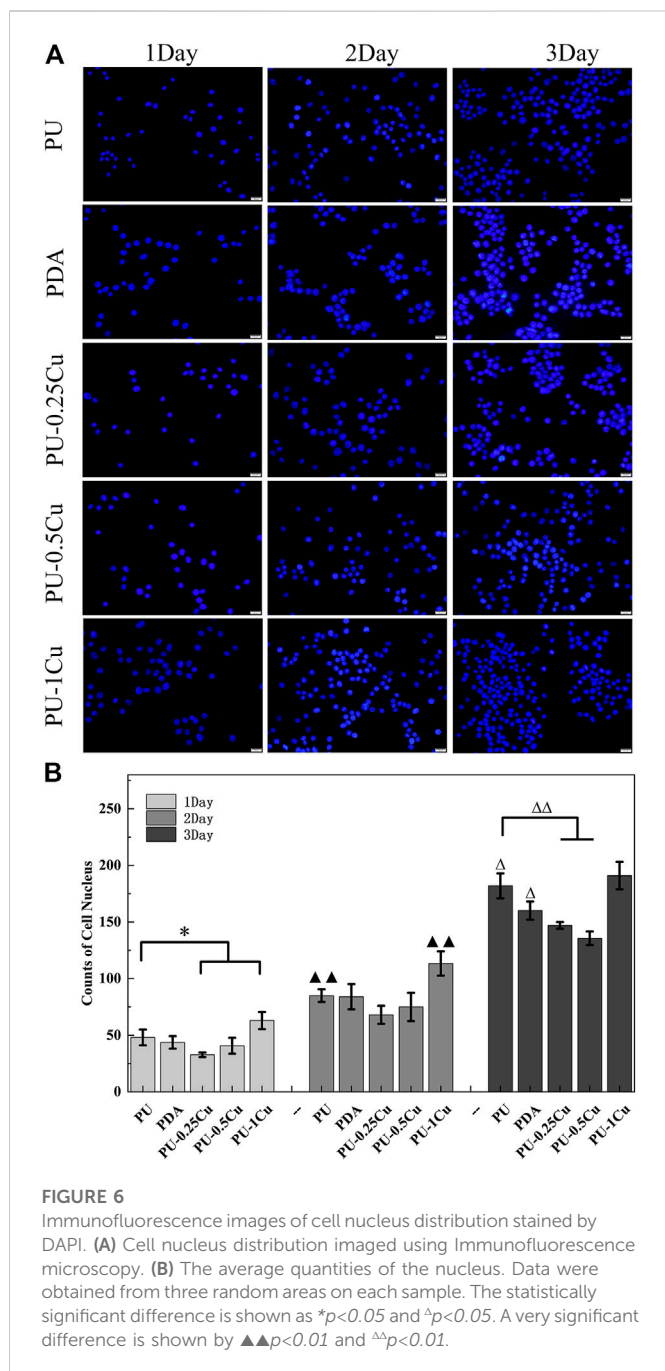$$\text{Relative Growth Rate} (\%) = \frac{A - B}{B} \times 100\%, \quad (2)$$

where *A* is *O.D.* for each experimental group and *B* is the control.

2.7 Annexin V-FITC/PI apoptosis assay

RAW264.7 cells at a density of 1×10^6 cells per well were incubated in a six-well plate with the sample extracts for 24 h, respectively. Trypsin solution with phenol red (EDTA-free) (Biosharp, China) was used to harvest the cells, then washed with ice-cold PBS, and re-suspended with Annexin V-FITC/PI apoptosis kit (Multisciences, China) according to the standard instructions. Afterward, flow cytometry was used to detect apoptosis of cells, and the corresponding data were analyzed using ModFit LT software.

2.8 Morphology of cells

RAW264.7 cells at a density of 1×10^4 cells were seeded on samples and incubated for 24, 48, and 72 h. Subsequently, substrates were fixed with 2.5% glutaraldehyde (Macklin, China) and dehydrated with serial concentrations of ethanol. After drying and gold spraying, SEM

FIGURE 6
Immunofluorescence images of cell nucleus distribution stained by DAPI. **(A)** Cell nucleus distribution imaged using Immunofluorescence microscopy. **(B)** The average quantities of the nucleus. Data were obtained from three random areas on each sample. The statistically significant difference is shown as *p<0.05* and △*p<0.05*. A very significant difference is shown by ▲▲*p<0.01* and △△*p<0.01*.

(TESCAN MIRA, Czech Republic) was used to observe morphology of macrophages.

2.9 Cell distribution

The cell nucleus stained by DAPI (Beyotime, China) was used to observe distribution and counts of RAW264.7 cells seeded on the samples and incubated for 24, 48, and 72 h. At the indicated time, samples were taken out and fixed with 4% paraformaldehyde (Biosharp, China) for 30 min and then supplemented with 0.1% Triton-X-100 (Dingguo, China) for 5 min. After washing with PBS, DAPI was used to stain the cells out of light. Three random areas on each sample were

observed using an immunofluorescence microscope (Olympus, Japan), and the average amount of cells was stated.

2.10 Wound healing assay

Wound healing assay was carried out to investigate the cell migration capacity of RAW264.7 cells. A density of 1×10^6 cells were cultured in a six-well plate and incubated until confluent. A 10-μL pipette tip was used to make a straight scratch. After washing three times, 2 mL of 24-h extracts was added, and photographs were taken using an optical microscope (Olympus, CKX53) at 0 h and after incubation for 24 h at a stable location. The wound areas were analyzed using Image J, and the relative migration area was calculated by the following equation:

$$\text{Relative Migration Area (\%)} = \frac{A - B}{A} \times 100\%, \qquad (3)$$

where A and B are the scratch marks with no cells at 0 and 24 h, respectively.

2.11 Transwell invasion assay

A measure of 100 μL of cell suspensions at a concentration of $5 \times 10^5/$ mL was added into the upper chambers and transferred to the wells of 24-well plates containing 600 μL DMEM or 24-h extracts supplemented with 10% FBS. After incubation for 36 h, the membrane was fixed with 4% paraformaldehyde for 30 min at 4 C and then was stained with 0.1% crystal violet (Lengene, China). Three random locations of the membrane were imaged using an optical microscope (Olympus, CKX53), and the migration numbers were quantified.

2.12 ELISA of IL-10 and IL-6

The secretion of pro- or anti-inflammatory cytokines (IL-6 and IL-10) of RAW264.7 was detected using the ELISA kit (Multisciences, China). RAW264.7 cells at a density of 1×10^5 cells per well were cultured in a six-well plate with the extracts for 24, 48, and 72 h. The collected specimen from each well was centrifuged at 1,000 rpm for 20 min, and the supernatant was measured using IL-6 and IL-10 ELISA kits, respectively, according to the manufacturer's protocol. The mean values of cytokine secretion of samples were calculated in triplicate.

2.13 Statistical analysis

Data were presented as mean ± standard deviation (SD). The statistical analysis was expressed by the *t*-test or one-way ANOVA with a *post hoc* test.

3 Results

3.1 XPS analysis

XPS was used to analyze the composition of substrates, and the corresponding spectra of N1s and Cu2p regions are shown in Figure 1A. A secondary amine (-NH-) with a binding energy of 399.5 *eV* appeared in
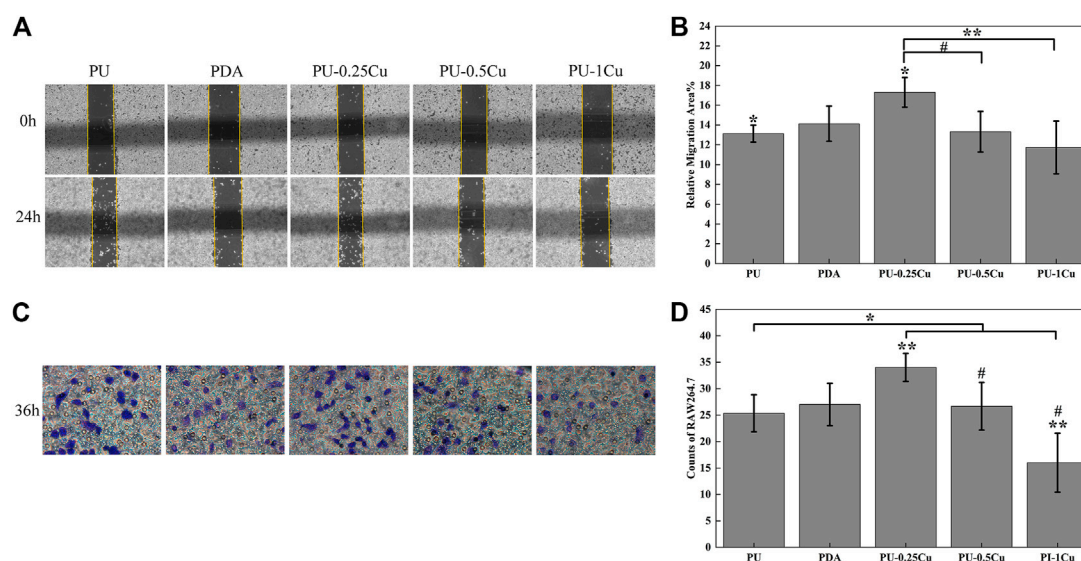
FIGURE 7
(A) Wound healing assay imaged using an optical microscope, magnified 100 times at 0 and 24 h. **(B)** Relative migration area of samples. **(C)** Transwell assay recorded using an optical microscope at 36 h. **(D)** Number of cells migrated through the membrane for 36 h. The statistically significant difference at $p<0.05$ is shown as *$p<0.05$ and #$p<0.05$. $p<0.01$ is shown by different letters **$p<0.01$.

PU, whereas an additional amino-rich tertiary group (=N-) with a binding energy of 398.5 eV, which was the characteristic peak of PDA, appeared in PU/PDA, indicating a successful coating of PDA on PU. The peaks of Cu2p, including Cu (932.50 eV) and CuO (934.60 eV), were considered important evidence to prove immobilization of Cu on the substrates as shown in Figure 1A (c)–(g). Table 2 depicts the proportion of Cu, which increases with concentrations of $CuCl_2$. The proportion of Cu loading on PU for concentrations of 0.25, 0.5, 1, 1.5, and 2 g/L were 11.98, 19.09, 24.61, 46.43, and 51.36%, respectively.

3.2 Topography and roughness

AFM was carried out to study surface topography and roughness of samples. The 3D images in Figure 1B depict that PU has a smooth surface; however, topography of Cu-loaded samples displays a certain fluctuation. It showed that Ra of PU was 1.61 ± 0.19 nm, which was enhanced after immobilizing copper, ranging from 5 to 7 nm with no significant difference.

3.3 Contact angles

As illustrated in Figure 1C, the contact angle of PU and PDA was 94.4° and 80.9°, respectively, indicating that PDA was successfully immobilized on PU with the help of a hydrophilic reagent. There was no significant difference in copper-loaded PU except for a slightly increasing tendency.

3.4 Antibacterial property

Figure 2A shows the antibacterial rate of samples cultured with *P. mirabilis* for 24 h. Compared to PU, an enormous improvement was seen in PU-Cu against microbes, increasing with the copper loading

content response. SEM was used to confirm adhesion of *P. mirabilis* on samples, as shown in Figure 2B. The morphology of *P. mirabilis* was rhabditiform and was distributed evenly on the majority of PU. However, fewer bacteria were adhered on PU-Cu samples.

3.5 Deposited encrustation assay

The primary elements of encrustation were Ca and Mg. It was shown that the concentrations of Ca^{2+} and Mg^{2+}, which dissolved from the samples, gradually decreased with the increasing contents of copper, as depicted in Figures 2C, D.

3.6 Cytotoxicity

CCK-8 was used to measure cytotoxicity of RAW264.7 after culturing with the extracts for 24, 48, and 72 h. As shown in Figure 3, the RGRs were all above 80% in PU, PDA, and PU-(0.25–1)Cu, indicating an acceptable cytotoxicity, according to the standard of ISO 10993–5. However, the RGR of cells co-cultured with PU-2Cu for 48 h was decreased to 66.71%, showing negative effects on RAW264.7 due to additional release of copper ions. When cultivating for 72 h, RGR was reduced to 59.68% and 57.30% for PU-1.5Cu and PU-2Cu, respectively, demonstrating that there was an acceptable cytotoxicity against cells only within a certain concentration range of Cu loaded on substrates. Thus, samples with an acceptable cytotoxicity were subjected to the following tests besides PU-1.5Cu and PU-2Cu.

3.7 Annexin V-FITC/PI apoptosis assay

Flow cytometry was performed to evaluate cell viability of PU, PDA, and PU-Cu groups. After incubating for 24 h, the results are
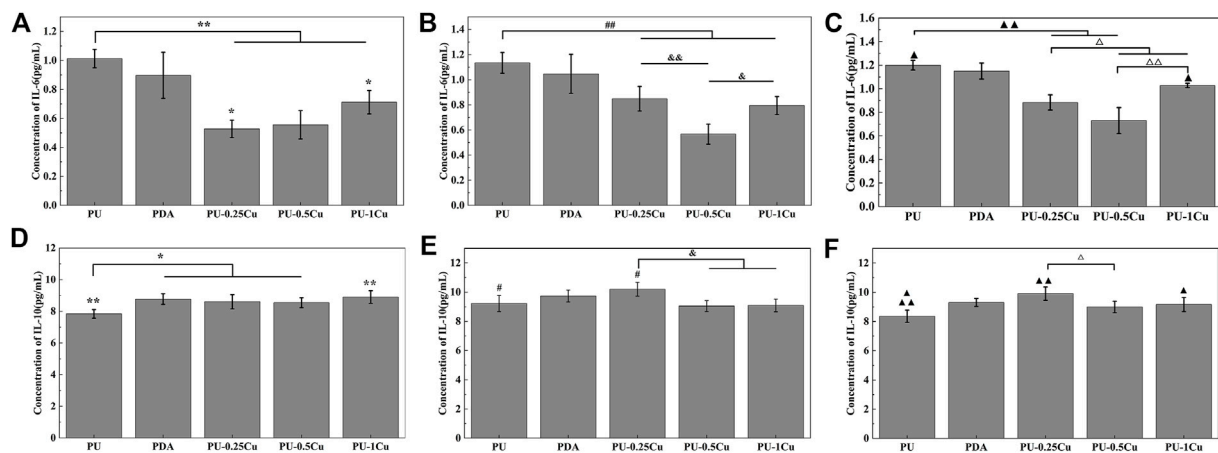
FIGURE 8
(A–C) Concentration of IL-6 secreted into the culture medium for 24, 48, and 72 h. Statistically significant differences are shown as *p<0.05, ᵇp<0.05, △p<0.05, ▲p<0.05, **p<0.01, ##p<0.01, ᵇᵇp<0.01, △△p<0.01, and▲▲p<<0.01. **(D–F)** Concentration of IL-10 secreted into the culture medium for 24, 48, and 72 h. Significant differences are represented as *p<0.05, #p<0.05, ᵇp<0.05, ▲p<0.05, △p<0.05 **p<0.01, and ▲▲p<0.01.

displayed in Figure 4. It could be concluded that the percentage of live cells (Q4) of PU was 75.7%, whereas that of PDA, PU-0.25Cu, PU-0.5Cu, and PU-1Cu was 74.3, 73.8, 72.2, and 75.7%, respectively.

3.8 Cell morphology

Cell morphology on the surface of samples was visualized by SEM. As shown in Figure 5, RAW264.7 cells on PU and PDA were activated to become spindle-shaped with more pseudopod spreading. However, the cells adhered on PU-Cu showed a spherical shape with almost no pseudopods, which means less effect on macrophage irritation. There was no significant discrepancy of cell morphology among Cu-loaded PU substrates.

3.9 Staining assay for the cell nucleus

Immunofluorescence microscopy was used to observe the cell nucleus distribution, and the corresponding results are shown in Figure 6. The average quantities of the nucleus were increased with the prolonged incubation period for each material. Statistically significant differences of PU-0.25Cu and PU-1Cu compared to PU indicated a favorable probability of cell attachment after coating with Cu for 24 h.

3.10 Cell migration assay

The effect of PU-Cu on cell migration capacities was investigated by wound healing and transwell assays, respectively. As presented in Figures 7A, B, the relative migration area of RAW264.7 incubated with PU-0.25Cu was 17.3%, which was significantly higher than that of PU (13.1%). However, the other PU-Cu samples showed a negative influence. In addition, Figures 7C, D illustrate cell longitudinal migration capacity evaluated by transwell assay. Similar to the results of wound healing and compared with PU or other PU-Cu samples, more stained cells were observed after incubating with PU-0.25Cu.

3.11 Detection of IL-6 and IL-10 secretion by ELISA

ELISA kits were used to detect concentrations of IL-6 and IL-10 secretion into the medium. As described in Figures 8A–C, the contents of IL-6 were obviously decreased after culturing with 24-h PU-Cu extracts, compared to PU for 24, 48, and 72 h. The concentration of the pro-inflammatory cytokine, IL-6, in PU was 1.013 ± 0.0064 pg/mL, whereas that in PU-0.25Cu, PU-0.5Cu, and PU-1Cu was 0.528 ± 0.060, 0.556 ± 0.098, and 0.712 ± 0.081 pg/mL, respectively, with the statistical difference between PU and PU-Cu for 24 h. It was obvious that the secretion of IL-6 in the PU group was increased to 1.200 ± 0.041 pg/mL after incubation for 72 h, while that of PU-Cu samples was significantly lower. These observations demonstrated that copper loaded on samples has a preferable effect on inflammatory inhibition. Figures 8D–F depict the concentration of IL-10 secreted into the medium. It can be seen that cells incubated with PU secreted the lowest concentration of IL-10 with a significant difference between PU-Cu for 24, 48, and 72 h, indicating that the anti-inflammatory cytokine, IL-10, would be increased with the existence of moderate Cu ions released from PU-Cu samples.
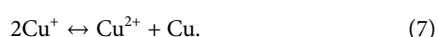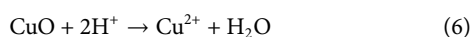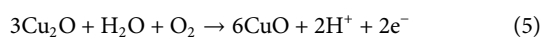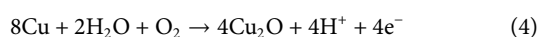
4 Discussion

Ureteral stents are indispensable in urological procedures and used to relieve obstruction after performing shock wave lithotripsy (Arkusz et al., 2021; Yoshida et al., 2021). Multiple serious effects attributing to the encrustation on stents coupled with subsequent chronic inflammatory response show an adverse influence on the recovery of patients (Rebl et al., 2020; Van de Perre et al., 2020). Thus, inhibitory inflammation is favorable to ureteral stents by modulating surface property. In this study, copper loaded on PU bound via PDA was conducted to kill microbes, contributing to the inhibition of encrustation formation, and suppressed the related cytokine expression for alleviating inflammatory response.

In order to confirm the coating of PDA on PU samples, high-resolution spectra of N1s were measured. The presence of a secondary

FIGURE 9
Schematic diagram of Cu-bearing stents, inhibiting encrustation *via* phagocytosis.
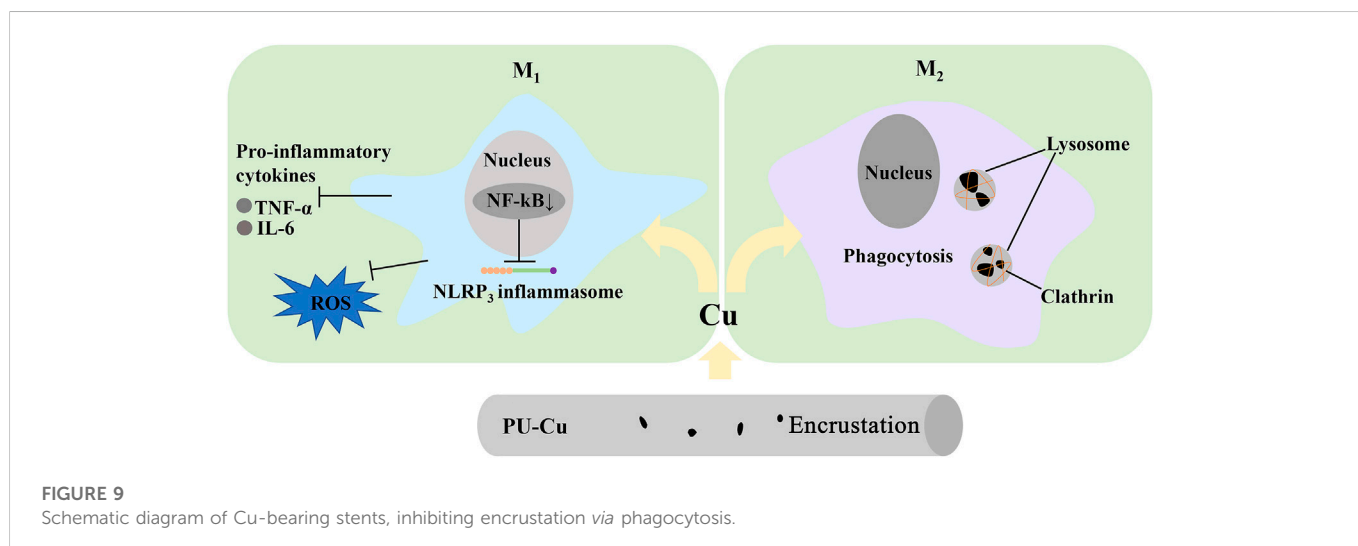
and tertiary amine group of PDA with binding energies of 399.5 *eV* and 398.5 *eV*, respectively, as shown in Figure 1A (b), indicated successful PDA deposition. Meanwhile, Cu and CuO peaks confirmed the successful immobilization of Cu on the substrates, as demonstrated by the roughness and hydrophilicity changes. Cu^+ is toxic to biological surroundings and kills bacteria via destroying Fe-S protein; however, it is not stable in solution as Cu^{2+}. The Cu-loaded samples reacted well with water and formed Cu_2O, which converted into CuO quickly (Eqs 4, 5) under an oxidation reaction. Cu^{2+} was then reproduced through the reaction with H^+ in urine, and the dynamic equilibrium would be broken by the action of Cu. Therefore, disproportionation reactions (Eqs 6, 7) could be restricted to form more Cu^+. Thus, in order to improve the antibacterial property, it is crucial to enhance the proportion of Cu on samples for more Cu^+. The SEM results showed the inhibitory performance of PU-Cu samples against *P. mirabilis* in Figure 2B. The majority of PU was distributed with microbes, while a decreased number of cells were adhered on PU-Cu samples with the enhanced Cu proportion. Furthermore, Ma et al. (2019) confirmed that the release of Cu ions on the urinary implant materials could kill microbes, thus blocking the occurrence of the deposited encrustation. The depositions on samples were dissolved with HCl, and the corresponding concentrations of Ca^{2+} and Mg^{2+} were analyzed by ICP-MS. A significant decrease of crystal deposition on PU-Cu samples compared to PU or PDA was shown, which was due to continuous contact with PU-Cu.

$$8Cu + 2H_2O + O_2 \rightarrow 4Cu_2O + 4H^+ + 4e^- \qquad (4)$$

$$3Cu_2O + H_2O + O_2 \rightarrow 6CuO + 2H^+ + 2e^- \qquad (5)$$

$$CuO + 2H^+ \rightarrow Cu^{2+} + H_2O \qquad (6)$$

$$2Cu^+ \leftrightarrow Cu^{2+} + Cu. \qquad (7)$$

However, it was indicated that PU-1.5Cu and PU-2Cu manifested certain cytotoxicity to macrophage compared to PU-(0.25–1)Cu, with the same toxic tendency with the proportion of Cu. Figure 3 shows that only an appropriate range of Cu is preferably vital for RAW264.7, affecting the regulating crystal deposition. Macrophages play a pivotal role in the inflammatory response, with the capability of phagocytosis and secretion of related inflammatory cytokines that are functional in immune defense

(Lee et al., 2021). The RAW264.7 cells were stimulated by samples to be activated and polarized to form pro-inflammatory M_1 macrophage or anti-inflammatory M_2 macrophage (Taguchi et al., 2016; Tu et al., 2021; Xiao et al., 2021). Pro-inflammatory M_1 macrophage enhances deposition of CaOx crystals and promotes tissue injury, whereas anti-inflammatory M_2 macrophage shows the opposite effect (Yang et al., 2020). Figure 5 confirms that the RAW264.7 cells adhered to PU were partly activated with the pseudopod spreading, whereas RAW264.7 cells on Cu-bearing samples were almost sphere plotting that showed anti-inflammatory tendency. In addition, macrophage recruitment and swallowing directly affect the eliminating crystals (Yan et al., 2022). Cell nucleus distribution as shown in Figure 6 was stained by DAPI, and the result identified that Cu ion plays an active role in RAW264.7 immobilization. Wound healing assay and transwell assay of cells indicated that RAW264.7 migrated faster and more with a certain concentration of Cu, which was conducive to enhancing chemotaxis. As mentioned previously, different secreted cytokines could promote inflammatory response or anti-inflammatory performance. ELISA for IL-6 secretion demonstrated that Cu can decrease secretion of the pro-inflammatory cytokine. However, it induced secretion of the anti-inflammatory cytokine, IL-10, suggesting that Cu modulated RAW264.7 for further immune response.

The mechanism of regulating encrustation response to macrophage is shown in Figure 9. M_1 and its corresponding pro-inflammatory cytokines, TNF-α and IL-6, and oxidative stress molecules, property to promote the development of CaOx stones, were downregulated *via* diminishing the nuclear factor kB (NF-kB) signal pathway after contacting with PU-Cu stents (Song et al., 2016; Liu et al., 2022a). Lysosome rupture, ROS generation, and NLRP3 inflammasome activation were blocked in the process of macrophage engulfing (Jin et al., 2011). Nevertheless, deposition of CaOx crystals was suppressed by PU-Cu through polarizing to M_2, which facilitates phagocytosis and contributes to eliminating crystals *via* lysosomes, clathrin mediation, and some related anti-inflammatory chemokines (Dominguez-Gutierrez et al., 2018; Taguchi et al., 2021). Further investigation should be focused on the related signal pathway targeting the regulation of macrophages converting into M_1 and M_2, and encrustation formation induced by the Cu-bearing ureteral stent in an infectious and crystal precipitation model.

5 Conclusion

In this study, Cu immobilized on PU was modified with the functionality of killing microbes and restraining encrustation. The antibacterial ability was increased with the concentration of Cu loading, whereas only PU-(0.25–1)Cu had an acceptable cytotoxicity to cells. In addition, RAW264.7 cells were recruited in the sustaining action of Cu and secreted the anti-inflammatory cytokine in response to phagocytized crystals, contributing to decreasing stone formation on the ureteral stent.

Data availability statement

The original contributions presented in the study are included in the article/Supplementary Material; further inquiries can be directed to the corresponding authors.

Author contributions

HL performed the experiments and investigation, analyzed the results, and drafted the manuscript. JZ revised the manuscript, approved the submitted version, and contributed to the design and conception of the study. ZW, JH, and BA searched for relevant literature works. JZ analyzed the results of the experiments. JL contributed to supervision, project administration, and acquisition of resources and management. LF performed acquisition of resources and management, supervision, and management of the project.

Conflict of interest

The authors declare that the research was conducted in the absence of any commercial or financial relationships that could be construed as a potential conflict of interest.

Publisher's note

All claims expressed in this article are solely those of the authors and do not necessarily represent those of their affiliated organizations, or those of the publisher, the editors, and the reviewers. Any product that may be evaluated in this article, or claim that may be made by its manufacturer, is not guaranteed or endorsed by the publisher.

References

Anders, H. J., Suarez-Alvarez, B., Grigorescu, M., Foresto-Neto, O., Steiger, S., Desai, J., et al. (2018). The macrophage phenotype and inflammasome component NLRP3 contributes to nephrocalcinosis-related chronic kidney disease independent from IL-1-mediated tissue injury. *Kidney Int.* 93 (3), 656–669. doi:10.1016/j.kint.2017.09.022

Arkusz, K., Pasik, K., Halinski, A., and Halinski, A. (2021). Surface analysis of ureteral stent before and after implantation in the bodies of child patients. *Urolithiasis* 49 (1), 83–92. doi:10.1007/s00240-020-01211-9

Barghouthy, Y., Wiseman, O., Ventimiglia, E., Letendre, J., Cloutier, J., Daudon, M., et al. (2021). Silicone-hydrocoated ureteral stents encrustation and biofilm formation after 3-week dwell time: Results of a prospective randomized multicenter clinical study. *World J. Urol.* 39 (9), 3623–3629. doi:10.1007/s00345-021-03646-0

Bhardwaj, M., and Ingole, N. (2022). Application, advancement, and complication of ureteral stent and encrustation: A major complication. *Cureus* 14 (8), e28639. doi:10.7759/cureus.28639

Dominguez-Gutierrez, P. R., Kusmartsev, S., Canales, B. K., and Khan, S. R. (2018). Calcium oxalate differentiates human monocytes into inflammatory M1 macrophages. *Front. Immunol.* 9, 1863. doi:10.3389/fimmu.2018.01863

Jiang, S., Wang, R., Han, L., Kuerban, K., Ye, L., Pan, S., et al. (2021). Activation of autophagy reverses gemcitabine-induced immune inhibition of RAW264.7 macrophages by promoting TNF-α, IL-6 and MHC-II expression. *Immunol. Res.* 69 (4), 352–362. doi:10.1007/s12026-021-09210-7

Jin, C., Frayssinet, P., Pelker, R., Cwirka, D., Hu, B., Vignery, A., et al. (2011). NLRP3 inflammasome plays a critical role in the pathogenesis of hydroxyapatite-associated arthropathy. *Proc. Natl. Acad. Sci. U. S. A.* 108 (36), 14867–14872. doi:10.1073/pnas.1111101108

Kram, W., Rebl, H., de la Cruz, J. E., Haag, A., Renner, J., Epting, T., et al. (2022). Interactive effects of copper-doped urological implants with tissue in the urinary tract for the inhibition of cell adhesion and encrustation in the animal model rat. *Polym. (Basel)* 14 (16), 3324. doi:10.3390/polym14163324

Lee, G. H., Kim, J. Y., Jin, S. W., Pham, T. H., Park, J. S., Kim, C. Y., et al. (2021). Impressic acid attenuates the lipopolysaccharide-induced inflammatory response by activating the AMPK/GSK3β/Nrf2 Axis in RAW264.7 macrophages. *Int. J. Mol. Sci.* 22 (2), 762. doi:10.3390/ijms22020762

Li, L. C., Pan, Z. H., Ning, D. S., and Fu, Y. X. (2020). Anti-inflammatory effect of simonsinol on lipopolysaccharide stimulated RAW264.7 cells through inactivation of NF-κB signaling pathway. *Molecules* 25 (16), 3573. doi:10.3390/molecules25163573

Li, X., Gao, H., Sun, X., Huang, Z., Wang, B., Li, Y., et al. (2021). A preliminary study on the role of Bacteroides fragilis in stent encrustation. *World J. Urol.* 39 (2), 579–588. doi:10.1007/s00345-020-03185-0

Liang, B., Wang, H., Wu, D., and Wang, Z. (2021). Macrophage M1/M2 polarization dynamically adapts to changes in microenvironment and modulates alveolar bone remodeling after dental implantation. *J. Leukoc. Biol.* 110 (3), 433–447. doi:10.1002/jlb.1ma0121-001r

Lin, Q., Li, S., Jiang, N., Shao, X., Zhang, M., Jin, H., et al. (2019). PINK1-parkin pathway of mitophagy protects against contrast-induced acute kidney injury via decreasing mitochondrial ROS and NLRP3 inflammasome activation. *Redox Biol.* 26, 101254. doi:10.1016/j.redox.2019.101254

Liu, H., Yang, X., Tang, K., Ye, T., Duan, C., Lv, P., et al. (2020). Sulforaphane elicts dual therapeutic effects on renal inflammatory injury and crystal deposition in calcium oxalate nephrocalcinosis. *Theranostics* 10 (16), 7319–7334. doi:10.7150/thno.44054

Liu, Y., Sun, Y., Kang, J., He, Z., Liu, Q., Wu, J., et al. (2022a). Role of ROS-induced NLRP3 inflammasome activation in the formation of calcium oxalate nephrolithiasis. *Front. Immunol.* 13, 818625. doi:10.3389/fimmu.2022.818625

Liu, Y., Wu, X., Fang, Q., Li, Z. X., Xia, G. Q., Cai, J. N., et al. (2022b). CD73 attenuates alcohol-induced liver injury and inflammation via blocking TLR4/MyD88/NF-κB signaling pathway. *J. Inflamm. Res.* 15, 53–70. doi:10.2147/jir.S341680

Ma, Z., Gao, M., Na, D., Li, Y., Tan, L., and Yang, K. (2019). Study on a biodegradable antibacterial Fe-Mn-C-Cu alloy as urinary implant material. *Mater Sci. Eng. C Mater Biol. Appl.* 103, 109718. doi:10.1016/j.msec.2019.05.003

Rebl, H., Renner, J., Kram, W., Springer, A., Fritsch, N., Hansmann, H., et al. (2020). Prevention of encrustation on ureteral stents: Which surface parameters provide guidance for the development of novel stent materials? *Polym. (Basel)* 12 (3), 558. doi:10.3390/polym12030558

Sali, G. M., and Joshi, H. B. (2020). Ureteric stents: Overview of current clinical applications and economic implications. *Int. J. Urol.* 27 (1), 7–15. doi:10.1111/iju.14119

Singhto, N., Kanlaya, R., Nilnumkhum, A., and Thongboonkerd, V. (2018). Roles of macrophage exosomes in immune response to calcium oxalate monohydrate crystals. *Front. Immunol.* 9, 316. doi:10.3389/fimmu.2018.00316

Singhto, N., and Thongboonkerd, V. (2018). Exosomes derived from calcium oxalate-exposed macrophages enhance IL-8 production from renal cells, neutrophil migration and crystal invasion through extracellular matrix. *J. Proteomics* 185, 64–76. doi:10.1016/j.jprot.2018.06.015

Song, H., Liu, B., Huai, W., Yu, Z., Wang, W., Zhao, J., et al. (2016). The E3 ubiquitin ligase TRIM31 attenuates NLRP3 inflammasome activation by promoting proteasomal degradation of NLRP3. *Nat. Commun.* 7, 13727. doi:10.1038/ncomms13727

Soria, F., de La Cruz, J. E., Fernandez, T., Budia, A., Serrano, Á., and Sanchez-Margallo, F. M. (2021). Heparin coating in biodegradable ureteral stents does not decrease bacterial colonization-assessment in ureteral stricture endourological treatment in animal model. *Transl. Androl. Urol.* 10 (4), 1700–1710. doi:10.21037/tau-21-19

Taguchi, K., Okada, A., Hamamoto, S., Unno, R., Moritoki, Y., Ando, R., et al. (2016). M1/M2-macrophage phenotypes regulate renal calcium oxalate crystal development. *Sci. Rep.* 6, 35167. doi:10.1038/srep35167

Taguchi, K., Okada, A., Unno, R., Hamamoto, S., and Yasui, T. (2021). Macrophage function in calcium oxalate kidney stone formation: A systematic review of literature. *Front. Immunol.* 12, 673690. doi:10.3389/fimmu.2021.673690

Tomer, N., Garden, E., Small, A., and Palese, M. (2021). Ureteral stent encrustation: Epidemiology, pathophysiology, management and current Technology. *J. Urol.* 205 (1), 68–77. doi:10.1097/ju.0000000000001343

Torrecilla, C., Fernández-Concha, J., Cansino, J. R., Mainez, J. A., Amón, J. H., Costas, S., et al. (2020). Reduction of ureteral stent encrustation by modulating the urine pH and inhibiting the crystal film with a new oral composition: A multicenter, placebo controlled, double blind, randomized clinical trial. *BMC Urol.* 20 (1), 65. doi:10.1186/s12894-020-00633-2

Tu, Y. J., Tan, B., Jiang, L., Wu, Z. H., Yu, H. J., Li, X. Q., et al. (2021). Emodin inhibits lipopolysaccharide-induced inflammation by activating autophagy in RAW 264.7 cells. *Chin. J. Integr. Med.* 27 (5), 345–352. doi:10.1007/s11655-020-3477-9

Van de Perre, E., Reichman, G., De Geyter, D., Geers, C., Wissing, K. M., and Letavernier, E. (2020). Encrusted uropathy: A comprehensive overview-to the bottom of the crust. *Front. Med. (Lausanne)* 7, 609024. doi:10.3389/fmed.2020.609024

Wasfi, R., Hamed, S. M., Amer, M. A., and Fahmy, L. I. (2020). *Proteus mirabilis* biofilm: Development and therapeutic strategies. *Front. Cell Infect. Microbiol.* 10, 414. doi:10.3389/fcimb.2020.00414

Xiao, L., Shiwaku, Y., Hamai, R., Tsuchiya, K., Sasaki, K., and Suzuki, O. (2021). Macrophage polarization related to crystal phases of calcium phosphate biomaterials. *Int. J. Mol. Sci.* 22 (20), 11252. doi:10.3390/ijms222011252

Xue, Y., Li, Q., Park, C. G., Klena, J. D., Anisimov, A. P., Sun, Z., et al. (2020). *Proteus mirabilis* targets atherosclerosis plaques in human coronary arteries via DC-SIGN (CD209). *Front. Immunol.* 11, 579010. doi:10.3389/fimmu.2020.579010

Yan, L., Chen, J., and Fang, W. (2022). Exosomes derived from calcium oxalate-treated macrophages promote apoptosis of HK-2 cells by promoting autophagy. *Bioengineered* 13 (2), 2442–2450. doi:10.1080/21655979.2021.2012622

Yang, X., Liu, H., Ye, T., Duan, C., Lv, P., Wu, X., et al. (2020). AhR activation attenuates calcium oxalate nephrocalcinosis by diminishing M1 macrophage polarization and promoting M2 macrophage polarization. *Theranostics* 10 (26), 12011–12025. doi:10.7150/thno.51144

Yoshida, T., Takemoto, K., Sakata, Y., Matsuzaki, T., Koito, Y., Yamashita, S., et al. (2021). A randomized clinical trial evaluating the short-term results of ureteral stent encrustation in urolithiasis patients undergoing ureteroscopy: Micro-computed tomography evaluation. *Sci. Rep.* 11 (1), 10337. doi:10.1038/s41598-021-89808-x

Zhao, J., Cao, Z., Lin, H., Yang, H., Li, J., Li, X., et al. (2019). *In vivo* research on Cu-bearing ureteral stent. *J. Mater Sci. Mater Med.* 30 (7), 83. doi:10.1007/s10856-019-6285-z

Zhu, W., Zhao, Z., Chou, F., Zuo, L., Liu, T., Yeh, S., et al. (2019). Loss of the androgen receptor suppresses intrarenal calcium oxalate crystals deposition via altering macrophage recruitment/M2 polarization with change of the miR-185-5p/CSF-1 signals. *Cell Death Dis.* 10 (4), 275. doi:10.1038/s41419-019-1358-y